

# Dual Feedback Attention Framework via Boundary-Aware Auxiliary and Progressive Semantic Optimization for Salient Object Detection in Optical Remote Sensing Imagery

Dejun Feng, Hongyu Chen, Suning Liu, Xingyu Shen, Ziyang Liao, Yakun Xie, Jun Zhu

**Abstract**—Salient object detection in optical remote sensing image (ORSI-SOD) has gradually attracted attention thanks to the development of deep learning (DL) and salient object detection in natural scene image (NSI-SOD). However, NSI and ORSI are different in many aspects, such as large coverage, complex background, and large differences in target types and scales. Therefore, a new dedicated method is needed for ORSI-SOD. In addition, existing methods do not pay sufficient attention to the boundary of the object, and the completeness of the final saliency map still needs improvement. To address these issues, we propose a novel method called Dual Feedback Attention Framework via Boundary-Aware Auxiliary and Progressive Semantic Optimization (DFA-BASO). First, Boundary Protection Calibration (BPC) module is proposed to reduce the loss of edge position information during forward propagation and suppress noise in low-level features. Second, a Dual Feature Feedback Complementary (DFFC) module is proposed based on BPC module. It aggregates boundary-semantic dual features and provides effective feedback to coordinate features across different layers. Finally, a Strong Semantic Feedback Refinement (SSFR) module is proposed to obtain more complete saliency maps. This module further refines feature representation and eliminates feature differences through a unique feedback mechanism. Extensive experiments on two public datasets show that DFA-BASO outperforms 15 state-of-the-art methods. Furthermore, this paper strongly demonstrates the true contribution of DFA-BASO to ORSI-SOD by in-depth analysis of the visualization figure. All codes can be found at <https://github.com/YUHss/DFA-BASO>.

**Index Terms**—Salient object detection, optical remote sensing image, edge, feature feedback, deep learning.

## I. INTRODUCTION

Salient object detection (SOD) is used to focus/locate the most salient regions in a scene by simulating the human visual system. Its application scenarios have been extended from natural images [1] to videos [2], RGB-D images [3], etc.,

This work was supported in part by the National Natural Science Foundation of China under Grant Nos. U2034202, 41871289 and 42201445, in part by the Sichuan Youth Science and Technology Innovation Team under Grant No. 2020JDTD0003. Dejun Feng and Hongyu Chen contributed equally. Yakun Xie is the corresponding author. (e-mail: yakunxie@163.com)

Dejun Feng is with the Faculty of Geosciences and Environmental Engineering, Southwest Jiaotong University, Chengdu 610097, China, also with the State-Province Joint Engineering Laboratory of Spatial Information Technology of High-Speed Rail Safety, Southwest Jiaotong University, Chengdu 610031, Sichuan, China (e-mail: djfeng@swjtu.edu.cn)

Hongyu Chen, Suning Liu, Xingyu Shen, Ziyang Liao, Yakun Xie and Jun Zhu are with the Faculty of Geosciences and Environmental Engineering, Southwest Jiaotong University, Chengdu 610097, China (e-mail: chy0519@my.swjtu.edu.cn; sakura\_ningning@163.com; sxyu@my.swjtu.edu.cn; LZYZ2021@my.swjtu.edu.cn; yakunxie@163.com; zhujun@swjtu.edu.cn).

and have been successfully applied in target tracking [4],[5], quality assessment [6],[7], image segmentation [8],[9], etc. With the improvement of the spatial resolution of optical remote sensing imagery (ORSI), SOD also has practical value in RSI, such as burn area extraction [10], real-time detection [11], and more. However, unlike NSI-SOD, ORSI covers a large area, has more complex backgrounds, contains numerous ground objects, in addition, the types and scales of target objects are quite different. Therefore, in order to enhance the analysis and understanding of the images, it is a challenging task to accurately discover salient objects from the ORSI.

Over the past few decades, numerous SOD methods have been proposed by researchers to accurately identify the most attractive regions in images. These methods can be broadly categorized into two types: traditional methods and deep learning (DL) methods. Traditional methods can be further divided into two categories: handcrafted feature-based methods and machine learning-based methods. Handcrafted feature-based methods mostly rely on classical principles to create handcrafted features, such as sparse representation[12],[13], feature fusion [14], and color information content [15]. Although this method has strong theoretical foundation, it may produce inaccurate detection results due to the presence of a large amount of noise around the target object in object-rich scenes of interest. With the accumulation of data, machine learning methods have been proposed by many researchers, which aim to obtain detection results by training classifiers such as random walks [16][17], support vector machine [18][19], conditional random field [20][21], etc. Although machine learning methods are more efficient than handcrafted feature-based methods, they are insufficient in learning deep-level features and cannot adapt well to complex ORSI. As shown in Fig. 1, both traditional methods failed to accurately focus on interest regions when facing ORSI with complex backgrounds.

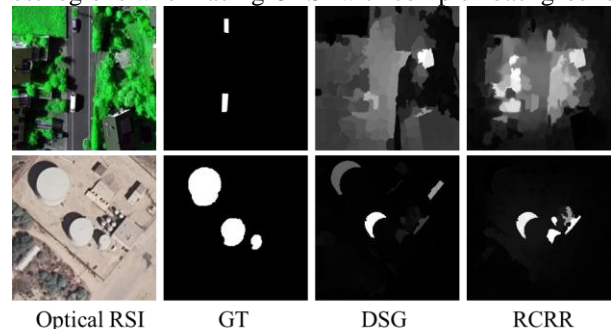


Fig. 1. Illustration of the performance of traditional methods.

In recent years, DL methods, especially those based on convolutional neural networks (CNNs), have rapidly developed. These methods can automatically extract and learn image features and achieve effective feature interaction as a way to cope with complex target structures and scenes in images. Therefore, numerous CNN-based models have been introduced into NSI-SOD [22]-[25], which not only improve the accuracy of SOD but also promote the development of SOD. However, NSI and ORSI are significantly different. NSI are generally captured using handheld camera by humans, while ORSI are captured at a high angle using satellites or aircraft. Thus, compared with NSI, ORSI have larger coverage area, and have great differences in target scale, complexity, orientation and brightness. In addition, there may be cases where there is no salient target for ORSI. Some representative scenarios are shown in Fig. 2. If the NSI-SOD method is migrated directly into ORSI it may make the detection results inaccurate. To address this issue, many researchers have proposed CNN models for ORSI-SOD with the increase in publicly available ORSI-SOD datasets. LVNet [26], one of the early works in ORSI-SOD, used nested connections to link detail and semantic features to suppress the interference of complex backgrounds. Subsequently, edge guidance [27], attention [28], and feature fusion [29] were also applied to ORSI-SOD to improve detection accuracy. For example, Zhou et al [30] proposed EMFINet, which directly fuses the feature layer with boundary information in the encoder with the last layer to generate boundary-aware features, and supervises them by a loss function. Zhou et al. [27] obtained boundary position features by fusing the encoder and decoder, while Zhang et al. [32] utilized dense attention to enhance saliency features.



**Fig. 2.** Examples of optical RSIs: (top row) optical RSIs and (bottom row) GT.

Although CNN-based ORSI-SOD methods have effectively improved detection accuracy, further analysis reveals that following limitations still exist in these methods.

(1) First, most of the existing methods [12], [26], [29], [33] ignore the influence of boundary contour information on detection results, which leads to blurry boundaries in the detection results. In order to capture detailed boundary information, the existing ORSI-SOD and NSI-SOD methods [34]-[37] generally use the output of encoding layers directly as boundary constraint information, without protecting and optimizing it. These methods can lead to interference of the results by the partial background noise that fills the low-level features. Alternatively, some methods incorporate boundary information into the loss function to guide the network to learn the contour details of salient objects. Furthermore, although high-level features contain rich semantics, they often lack accurate positional information. Therefore, how to make the

location information and semantic information complement each other among the layers, and thus to include multi-level features in each layer, is also a problem that needs to be solved by existing methods.

(2) Second, most of the existing methods [38]-[40] have not paid enough attention to the last decoding layer, and the decoder structure is relatively simple. Generally, these methods directly aggregate information from different layers or even use a single layer to output the saliency map. However, there may be missing and redundant information at different levels and the single output is even more lacking in multi-scale feature representation. Specifically, the last layer is generally closest to the ground truth, and if it can be used to optimize the missing features at different levels, a richer multi-level contextual information with accurate feature representation can be obtained.

(3) Finally, most of the existing methods [27], [35], [59] only judged by quantitative analysis or qualitative analysis when analyzing the contribution of the proposed method, without deeply exploring the true contribute of each module for ORSI-SOD.

After the above detailed analysis, we propose a novel method dedicated to ORSI-SOD called Dual Feedback Attention Framework via Boundary-Aware Auxiliary and Progressive Semantic Optimization (DFA-BASO). The motivation behind this method is twofold. First, the existing methods cannot protect the boundary information in the low-level features well, which makes the more accurate boundary information lost in the feature transfer process or makes the boundary information retained in the high-level features too little, while the low-level features contain a lot of uncertain noise. Second, existing methods do not give enough attention to the last layer of the network. When aggregating multi-scale information, different-scale features have a certain semantic gap, making it difficult to generate more precise results. Our main contributions are as follows.

(1) A novel method specifically for ORSI-SOD, DFA-BASO, is proposed, which aims to explore edge cues of salient objects, enhance the representation of details in saliency maps, and suppress the differences between features to obtain more accurate results. Particularly, extensive comparative experiments and analyses have demonstrated that DFA-BASO outperforms 15 other state-of-the-art methods on two publicly available datasets, and the effectiveness of the proposed module has been validated through detailed visualization of feature maps.

(2) We designed a Boundary Protection Calibration Module (BPC) for the encoder, which consists of two sub-modules, where the adjacent feature attention (AFA) sub-module integrates the adjacent features to enhance the representation of boundary location features, while the feature calibration (FC) sub-module gradually calibrates low-level features to highlight edge clues. A progressive optimization approach is adopted to suppress the significant loss of edge information during forward propagation.

(3) Two unique feedback methods are introduced to the encoder and decoder, in the encoder, the Dual Feature Feedback

Complementary (DFFC) Module feeds back the captured boundary-semantic dual features to coordinate and complement features at all levels. In the decoder, the Strong Semantic Feedback Refinement (SSFR) Module is designed to suppress inter-feature differences and provide value information to obtain a more fine-grained salient map, considering the uniqueness of the last layer.

(4) In order to better facilitate the subsequent research of SOD, we provide a public code base which has 16 SOD methods, including 6 ORSI-SOD methods, 7 NSI-SOD methods, 2 traditional SOD methods and the method proposed in this paper. To the best of our knowledge, this is the first codebase that integrates numerous SOD methods.

## II. RELATED WORK

In this section, we summarize the traditional SOD methods and DL-SOD methods in both natural and optical scenes.

### A. SOD in Natural Scenes

(1) *Traditional Methods:* SOD was initially applied in NSI. Itti et al. [42] proposed the center-surround difference theory, which was a groundbreaking work, and numerous theory-based methods were subsequently proposed. For example, Ren et al. [43] integrated region contrast, depth, and orientation priors to achieve SOD. Wang et al. [44] proposed a supervised multiple instances learning framework for SOD and utilized low-, mid-, and high-level features for testing. Wei et al. [45] used background priors in NSI to provide more clues for SOD. With the maturity of technology, numerous traditional machine learning methods have also been applied in this field. For instance, Liu et al. [46] used conditional random fields to combine numerous features for SOD, and Jiang et al. [47] used the random forest method to map feature vectors to saliency scores. In [19], an SVM-based method was proposed to generate complementary saliency maps. Similarly, in [18], multiple SVM results were integrated to obtain the final saliency result. Although these traditional methods have strong theoretical foundations, most of them are based on handcrafted features and often fail in complex and cluttered scenes.

(2) *Deep Learning-Based Methods:* In recent years, given the advantages of DL methods in the field of computer vision, more and more researchers have applied it to SOD, significantly promoting the development of the SOD. Li and Yu [48] used three convolutional branches to extract multi-scale depth features on images with different resolutions, optimizing the saliency results and spatial consistency. This was the pioneering work of applying DL methods to SOD. Subsequently, Deng et al. [49] proposed R3Net, which uses residuals to obtain complementary saliency information and refines the saliency map with residuals to obtain more accurate salient regions. Hu et al. [50] proposed a fully convolutional network (FCN) with cyclic aggregated deep features for salient object detection, using multi-level features in a recursive manner to gradually refine the depth features of each layer. Wu et al. [51] proposed a decoder that discards larger-resolution features from shallow layers and directly uses the generated saliency map to optimize the network, effectively suppressing interference. Chen et al.

[52] used a discriminative cross-modal transfer learning network for RGB-D SOD. In addition, edge details in the saliency map are important information, and now many models consider using edge information as auxiliary information to obtain fine contour details. In [33], BASNet, a prediction-refinement architecture, and a mixed loss focusing on edges were proposed to improve attention to edges in the saliency map. In [34], EGNNet was proposed to study the complementarity between boundary information and objects. Sun et al. [53] proposed BGNNet to explore object-related edge information. Although these DL-based methods can achieve good results in SOD, there are certain differences between NSI and ORSI, and if forced migration is performed, it often has a negative effect.

### B. SOD in Optical Scenes

(1) *Traditional Methods:* As a result of the importance of ORSI and SOD, research on ORSI-SOD has gradually increased. Traditional methods for RSI-SOD are similar to unsupervised NSI-SOD models. For example, Faur et al. [54] described image segmentation as an attempt to find the best possible representation of an image using a certain number of "objects". They considered RSI-SOD to be a data compression technique and proposed a method based on rate-distortion measures. In [12], sparse representation was used to obtain global and background information for generating saliency maps. Ma et al. [55] yielded feature maps using structure tensors and background contrast, which were then fused to produce super pixel saliency map. Liu et al. [56] constructed a colored Markov chain and combined the latent saliency map with circular feature maps to generate the best saliency map. However, it is worth noting that the rapid development of DL has made the traditional ORSI-SOD method is becoming less and less.

(2) *DL-Based Methods:* As DL-based methods become increasingly popular, researchers are exploring DL-based methods for RSI-SOD. Dong et al. [57] designed a multi-scale pyramid structure to generate saliency maps and used them to construct a graph-based segmentation. Cong et al. [28] proposed the Relationship Reasoning Network (RRNet), which effectively recovers detailed information and addresses the scale variation problem of salient objects. Li et al. [58] proposed an Adjacent Context Coordination Network (ACCoNet), which enhances salient regions and coordinates multi-level features by introducing adjacent level global information. Li et al. [59] proposed a lightweight RSI-SOD network, CorrNet, which reduces the backbone (VGG-16) and constructs a lightweight subnet for feature extraction. To explore the complementary nature of multi-content in RSI-SOD and highlight salient regions at different scales in RSI features through an attention mechanism, Li et al. [37] proposed a new Multi-Content Complementary Network (MCCNet). Tu et al. [60] proposed an ORSI saliency detection model based on a multi-scale joint region and boundary model, which focuses on solving problems such as background clutter, illumination shadow, imaging blur, and low resolution. To address the challenges of complex types and diverse scales, Liu et al. [61] proposed a Global Perception Network (GPNet). Moreover,

since ORSI objects contain more complex edges, researchers have started paying attention to how to accurately obtain the edge information of salient objects in ORSI. For example, Zhou et al. [27][35] introduced boundary information to obtain more precise saliency maps and successively proposed the edge-aware multiscale feature integration network (EMFI-Net) and the edge-guided recurrent positioning network (ERPNet).

### III. METHODOLOGY

#### A. Overview

The overall framework of DFA-BASO is shown in Fig. 3, which consists of five parts: Encoder, Boundary Protection Calibration (BPC) module, Dual Feature Feedback Complementary (DFFC) module, Decoder, and Strong Semantic Feedback Refinement (SSFR) module. First, we use

VGG16 [41] as the basic backbone for initial feature extraction, and we remove its last four layers compared with VGG16 for the classification task. If the input image is  $E \in \mathbb{R}^{3 \times H \times W}$ , after passing through the backbone is changed  $E \in \mathbb{R}^{512 \times \frac{H}{16} \times \frac{W}{16}}$ . Secondly, BPC module is used to protect the boundary information during the backward propagation process and learn the offset of information between adjacent layers, which further calibrates the boundary position information. Then, DFFC module is used to supplement the features of each layer of the encoder, so that it contains both rich semantics and accurate boundary information. Finally, in order to obtain a more refined saliency map, SSFR module is used to optimize and correct the multi-level features of the decoder. In the following sections, we will introduce the details of each module in detail.

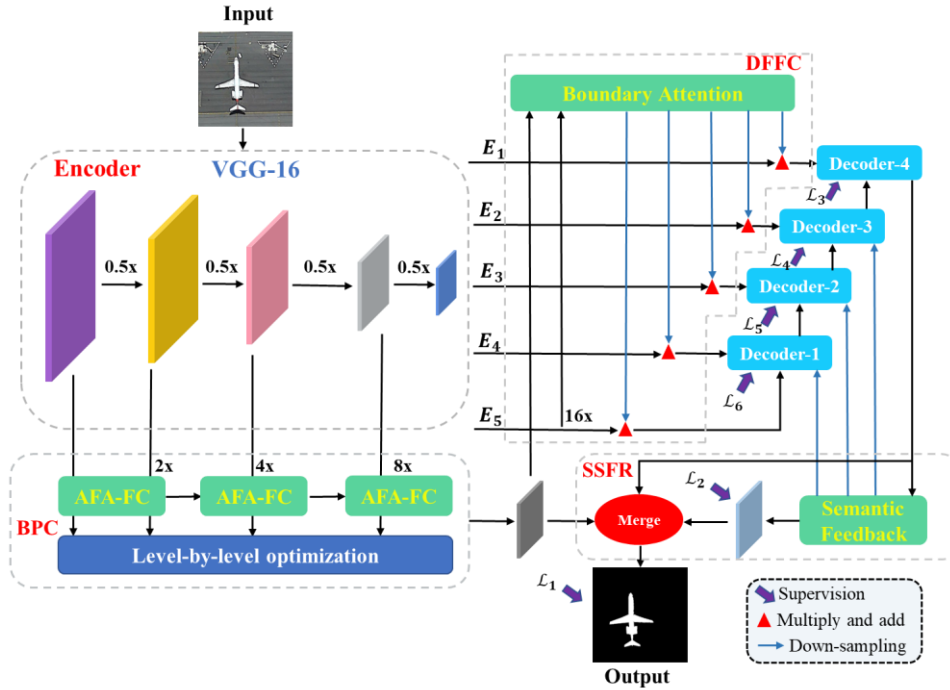


Fig. 3. Architecture of the proposed DFA-BASO.

#### B. Boundary Protection Calibration Module

To prevent significant loss of boundary position information during forward propagation, inspired by Cheng et al. [62], we believe that the loss of boundary information during

transmission from shallow to deep can be mitigated by progressive protection optimization of low-level features. Based on this, we propose the BPC module, which has the overall framework shown in Fig. 4. We will describe the module in detail in three steps.

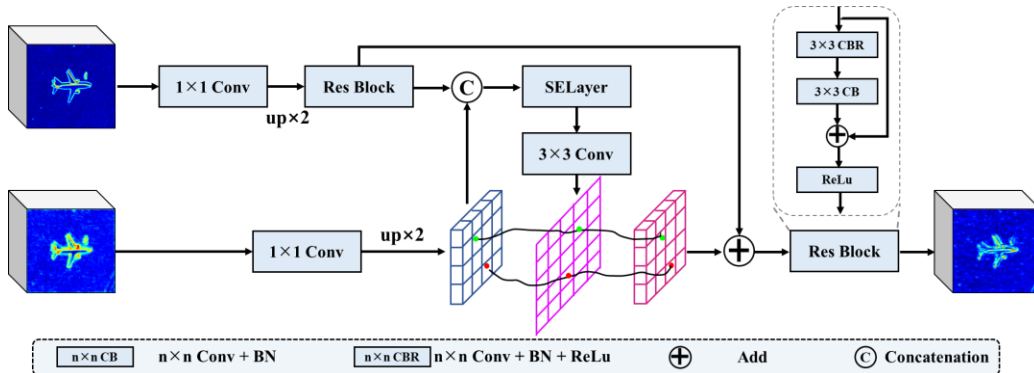


Fig. 4. The overall architecture of the proposed BPC.

(1) *Adjacent feature attention (AFA) sub-module*: First, we upsample the first two layers of adjacent features of the encoder (i.e.,  $E_i \{i = 1, i = 2\}$ ) by a bilinear interpolation method to obtain  $E_i^{up} \in \mathbb{R}^{3 \times H \times W} \{i = 1, i = 2\}$ . Second,  $E_i^{up} \{i = 1\}$  is optimized through a residual module consisting of two convolutional blocks, and the captured features can be denoted as  $f_i^{res} \{i = 1\}$ . Finally, we integrate the adjacent feature layer information by concatenating  $f_i^{res} \{i = 1\}$  and  $E_i^{up} \{i = 2\}$ . We then enhance the perception and attention to low-level feature information using the SELayer [63] to obtain more accurate boundary information. The entire process can be described as.

$$f_a = SE(Cat(Res(Up(E_1)), Up(E_2)))$$

where  $f_a$  represents the output feature map  $f_a \in \mathbb{R}^{128 \times H \times W}$ ;  $SE(\cdot)$  denotes the SELayer;  $Cat(\cdot)$  denotes the concatenate operation;  $Res(\cdot)$  denotes the residual module;  $Up(\cdot)$  denotes the upsampling operation;  $E_1, E_2$  represent the first two layers of VGG16.

(2) *Feature calibration (FC) sub-module*: In order to better protect the encoder boundary location information and calibrate it level by level, we try to obtain the semantic offsets between adjacent feature layers. First, based on the obtained adjacent feature information  $f_a$ , the number of channels is further reduced to 2 by using a 3x3 convolution to obtain the semantic offset  $f_a^1 \in \mathbb{R}^{2 \times H \times W}$ . It is worth noting that  $f_a^1$  is obtained by calculating the flow field between the adjacent feature layers (i.e.,  $f_1^{res}$  and  $E_2^{up}$ ). The process can be represented as follows.

$$f_a^1 = Conv_{3 \times 3}(f_a)$$

where  $Conv_{3 \times 3}(\cdot)$  represents the 3x3 convolution operation. Then, based on the obtained semantic offset  $f_a^1$ , we can iterate through each pixel in  $E_2^{up}$  and remap it to a grid of the same size as the Flow Field. Afterwards,  $f_1^{res}$  will be fused with more accurate features generated by remapping. Through this process, the network can perform more accurate feature propagation and gradually correct the boundary position information captured by shallow layers. The calibration process can be described as.

$$I_1 = GS(E_2^{up}, f_a^1) \oplus f_1^{res}$$

where  $GS(\cdot)$  represents grid sampling;  $E_2^{up}$  represents the upsampled result of the second feature layer in the encoder;  $f_a^1$  is the semantic offset;  $f_1^{res}$  represents the result of the first feature layer in the encoder refined by residual blocks, and  $\oplus$  denotes the addition operation.

(3) *Level-by-level optimization*: Building upon (1) and (2),  $I_1$  is fed into the same residual block as that in (1), and  $E_i \{i = 3\}$  is upsampled to obtain  $E_i^{up} \{i = 3\}$ . The information from both is integrated, and the flow field between  $f_1^{res}$  and  $E_3^{up}$  is computed using the same approach to obtain the semantic offset. This offset is then remapped to correct the features of  $E_3$  and  $E_4$ , similar to the process between  $f_1^{res}$  and  $E_3^{up}$ . With this level-by-level optimization, more precise boundary information can be obtained. It is noteworthy that only the first four layers of the encoder are used for optimization since the boundary position information is more apparent in these layers compared with the last layer. The process of level-by-level optimization

can be expressed as.

$$\begin{cases} I_1 = GS(E_2^{up}, f_a^1) \oplus f_1^{res} \\ I_2 = GS(E_3^{up}, f_a^2) \oplus I_1 \\ I_3 = GS(E_4^{up}, f_a^3) \oplus I_2 \end{cases}$$

where  $I_i \{i = 1, 2, 3\}$  denotes the results after correction;  $GS(\cdot)$  represents the grid sampling;  $E_i^{up} \{i = 2, 3, 4\}$  denotes the corresponding upsampling operation of feature layers;  $f_a^i \{i = 1, 2, 3\}$  represents the semantic offset between adjacent layers after (1);  $f_1^{res}$  denotes the refined result of the first feature layer in the encoder by residual blocks, and  $\oplus$  represents the element-wise addition. The saliency map outputted by the BPC module is finally denoted as  $\mathcal{M}_1 \in \mathbb{R}^{64 \times H \times W}$

### C. Dual Feature Feedback Complementary Module

The last layer of the encoder usually has a strong semantic information. Therefore, based on the accurate boundary information captured by the BPC module, boundary-semantic dual features can be used to supplement the feature information of each layer of the encoder. To achieve this, a DFFC module is proposed, which is detailed in Fig. 3.

First, the boundary information  $I_3$  corrected in B (2) is fused with the feature information of the last encoder layer  $E_5$ . Subsequently, the boundary-semantic dual-feature attention map is obtained through the sigmoid function. This process can be expressed as

$$\begin{aligned} \mathcal{P} &= Cat(I_3, Up(Conv_{1 \times 1}(E_5))) \\ \mathcal{P}' &= \sigma(Conv_{1 \times 1}(\mathcal{P})) \end{aligned}$$

where  $Cat(\cdot)$  denotes the concatenate operation;  $Up(\cdot)$  represents upsampling;  $Conv_{1 \times 1}(\cdot)$  denotes a 1x1 convolution, and  $\sigma(\cdot)$  represents the sigmoid function.

Finally, in order to enable efficient feedback transfer of the attention map, the attention map  $\mathcal{P}'$  is directly downsampled to the same size as each feature maps in the encoder before multiplying and adding. This operation is used to effectively complement the features of each layer. Besides, the SELayer, which enriches the dual-feature information (i.e., semantic and boundary information) in layers of encoder, is used after each feedback to strengthen attention to important information. The entire process is expressed as follows.

$$G_i = SE((DS(E_i) \oplus 1) \otimes E_i)$$

where  $E_i$  represents the feature maps of the encoder layers, with  $i = 5, \dots, 1$ ;  $DS(\cdot)$  denotes downsampling;  $SE(\cdot)$  represents the SELayer;  $\oplus$  denotes element-wise addition, and  $\otimes$  denotes element-wise multiplication.

### D. Strong Semantic Feedback Refinement Module

Most current SOD methods ignore the importance of the last layer in the decoder. While BPC module and DFFC module can make the feature map information of different layers relatively diverse, they are not capable of completely eliminating the redundant information and noise produced by the encoder. Therefore, in order to obtain more accurate saliency maps and effectively alleviate these problems, we introduce a novel SSFR module, specific details are shown in Fig. 5.

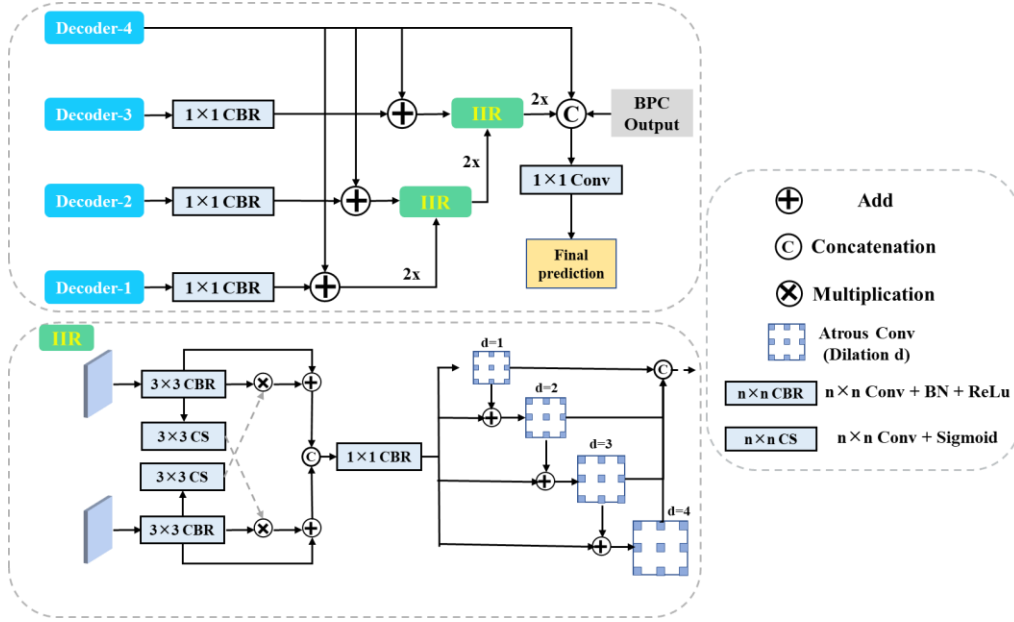


Fig. 5. Architecture of the proposed DFFC.

(1) *Feedback details*: In order to obtain more complete features at each level of the decoder and output more accurate saliency map, we first directly downsample the last decode layer to the same size as the other three layers to obtain three feedback features:  $\mathcal{FB}_1 \in \mathbb{R}^{64 \times \frac{H}{8} \times \frac{W}{8}}$ ,  $\mathcal{FB}_2 \in \mathbb{R}^{64 \times \frac{H}{4} \times \frac{W}{4}}$ , and  $\mathcal{FB}_3 \in \mathbb{R}^{64 \times \frac{H}{2} \times \frac{W}{2}}$ , and refine the features of each layer by feeding forward in turn. Simply put,  $\mathcal{FB}_i \{i = 1, 2, 3\}$  are integrated with the corresponding feature maps of the same size, which can be described as.

$$\mathcal{F}_i = \mathcal{FB}_i + \text{Conv}_{1 \times 1}(\mathcal{D}_i) \{i = 1, 2, 3\}$$

where  $\mathcal{F}_i$  represents the preliminary feature maps after feedback,  $\mathcal{FB}_i$  represents the downsampled feedback feature maps,  $\text{Conv}_{1 \times 1}(\cdot)$  represents the 1x1 convolution block, which includes BN and ReLU, and  $\mathcal{D}_i$  represents the other three layers of the decoder.

(2) *Inter-layer information refinement (IIR) sub-module*: The inter-feature differences are suppressed considering that there is some difference in the information contained between the layers and in order to be able to capture the rich contextual information between different scales. First, we generate attention maps  $\mathcal{A}_1$  and  $\mathcal{A}_2$  by applying the sigmoid function to  $\mathcal{F}_1$  and  $\mathcal{F}_2$ , respectively. Mathematically, this process can be expressed as follows:

$$\mathcal{A}_i = \sigma(\text{Conv}_{3 \times 3}(\text{Conv}_{3 \times 3}(\mathcal{F}_i))) \{i = 1, 2\}$$

where  $\sigma(\cdot)$  denotes the Sigmoid function,  $\text{Conv}_{3 \times 3}(\cdot)$  represents a 3x3 convolution operation, and  $\mathcal{F}_i$  denotes the preliminary feature maps obtained after feedback.

Next, the feature of each layer is complementarily refined by cross-multiplying and adding to minimize the feature differences between the various layers prior to merging. This process can be described as follows.

$$\mathcal{C}_1 = \text{Conv}_{3 \times 3}((\mathcal{A}_1 \oplus 1) \otimes \text{Conv}_{3 \times 3}(\mathcal{F}_2))$$

$$\mathcal{C}_2 = \text{Conv}_{3 \times 3}((\mathcal{A}_2 \oplus 1) \otimes \text{Conv}_{3 \times 3}(\mathcal{F}_1))$$

$$\mathcal{S} = \text{Conv}_{1 \times 1}(\text{Cat}(\mathcal{C}_1, \mathcal{C}_2))$$

where  $\mathcal{C}_i \{i = 1, 2\}$  represents the cross-refined feature maps,  $\text{Conv}_{3 \times 3}(\cdot)$  and  $\text{Conv}_{1 \times 1}(\cdot)$  denote 3x3 and 1x1 convolutions, respectively.  $\mathcal{A}_i \{i = 1, 2\}$  represents attention maps,  $\mathcal{F}_i \{i = 1, 2\}$  denotes preliminary feature maps after feedback, and  $\mathcal{S}$  represents the merged feature map. The symbol  $\oplus$  denotes element-wise addition, while  $\otimes$  represents element-wise multiplication.

Finally, as depicted in Fig. 5, a dense connectivity approach is employed to capture contextual information at various scales. Four dilated convolutions are parallelly connected with increasing dilation rates (1, 2, 3, and 4) to gradually enlarge the receptive field and extend the "visual scope" of the network to cover a larger range. Notably, for  $\mathcal{D}_3$ , we cross-learn it with the results of the first two feedback refinements in a process consistent with that described above. The decoder layers are gradually refined with these three rounds of feedback optimization, resulting in more accurate saliency maps.

(3) *Information fusion and deep supervision strategy*: Further information fusion is performed to improve the completeness of the final saliency map. Specifically, we integrate the last layer of the decoder, the boundary information  $I_3$  corrected in B(2), and the refined results obtained by semantic feedback. Then, we obtain the final output through a 1x1 convolution. Moreover, a deep supervision strategy [64] is adopted to ease the training of the shallow layers and mitigate gradient explosion or disappearance. More precisely, we use a 1x1 convolution to generate an output at the end of each of the four decoder stages and after the D(2) process.

## IV. EXPERIMENTS

### A. Datasets and Implementation Details

(1) *Datasets*: The proposed method is trained and tested on two publicly available ORSI-SOD datasets.

**ORSSD** [26]: The dataset consists of 800 ORSIs with corresponding pixel-level annotations, including 600 training

images and 200 testing images.

**EORSSD** [31]: The dataset expands the original ORSSD dataset to 2000 ORSIs with corresponding pixel-level ground truth. It contains 1400 training images with corresponding labels and 600 testing images with corresponding labels.

(2) *Implementation Details*: All experiments are performed on a server equipped with NVIDIA GeForce RTX 3090 24G. Adam optimizer is used with a learning rate of  $1e-4$  and a batch size of 8. The models are trained for 50 epochs on ORSSD and 45 epochs on EORSSD, with the learning rate multiplied by 0.1 after every 40th epoch. In addition, each image is resized to  $256 \times 256$  before inputting due to the memory limitations. To prevent overfitting during the training process, a series of data augmentation strategies, such as random rotation, horizontal and vertical flipping, grid distortion, and Gaussian blurring are introduced.

### B. Comparison with State-of-the-Art Methods

The proposed method is compared with 15 state-of-the-art

methods on two datasets, including two traditional methods (i.e., DSG [13], RCNN [17]), seven NSI-SOD methods (i.e., SCRNet [65], CPDNet [51], GateNet [66], CTDNet [67], PFSNet [68], BSANet [69], PGNet [70]), and six ORSI-SOD methods (i.e., FSMINet [71], ERPNet [27], CorrNet [59], ACCoNet [58], EMFINet [35], JRBM [60]). For a fair comparison, all saliency maps are obtained using the original code from authors, and all networks are retrained on the two datasets.

(1) *Quantitative Analysis*: Table I presents a quantitative comparison of our method and other methods on two datasets using eight common SOD evaluation metrics, including Mean Absolute Error Value ( $\mathcal{M}$ ) [72], S-measure Value ( $S_\alpha$ ) [73], E-measure Value ( $E_\xi$ ) [74], and F-measure Value ( $F_\beta$ ) [75]. For  $E_\xi$  and  $F_\beta$ , we record their adaptive value ( $E_\xi^{adp}$  and  $F_\beta^{adp}$ ), mean value ( $E_\xi^{mean}$  and  $F_\beta^{mean}$ ), and maximum value ( $E_\xi^{max}$  and  $F_\beta^{max}$ ). For all metrics except  $\mathcal{M}$ , higher values indicate better performance.

TABLE I

QUANTITATIVE COMPARISON RESULTS ON THE ORSSD AND EORSSD DATASETS. HERE, “ $\uparrow$ ” ( $\downarrow$ ) MEANS THAT THE LARGER (SMALLER) THE BETTER. THE BEST THREE RESULTS IN EACH ROW ARE MARKED IN RED, BLUE, AND GREEN, RESPECTIVELY

Methods	Publication	ORSSD								EORSSD							
		$\mathcal{M} \downarrow$	$S_\alpha \uparrow$	$E_\xi^{adp} \uparrow$	$E_\xi^{mean} \uparrow$	$E_\xi^{max} \uparrow$	$F_\beta^{adp} \uparrow$	$F_\beta^{mean} \uparrow$	$F_\beta^{max} \uparrow$	$\mathcal{M} \downarrow$	$S_\alpha \uparrow$	$E_\xi^{adp} \uparrow$	$E_\xi^{mean} \uparrow$	$E_\xi^{max} \uparrow$	$F_\beta^{adp} \uparrow$	$F_\beta^{mean} \uparrow$	$F_\beta^{max} \uparrow$
Traditional methods																	
DSG	TIP 2017	.1024	.7186	.7538	.7331	.7849	.5655	.5682	.6090	.1250	.6423	.6269	.6590	.7286	.3946	.4580	.5233
RCNN	TIP 2018	.1277	.6849	.6957	.7021	.7651	.4876	.5127	.5591	.1647	.6011	.5658	.5953	.6878	.3371	.3704	.4018
DL-based NSI-SOD methods																	
SCRNet	ICCV 2019	.0166	.8951	.9079	.9261	.9523	.7534	.8296	.8623	.0174	.8490	.7763	.8835	.9366	.5696	.7429	.7898
CPDNet	CVPR 2019	.0187	.8954	.9211	.9207	.9438	.7717	.8243	.8524	.0111	.8874	.8663	.8977	.9390	.6638	.7660	.8093
GateNet	ECCV 2020	.0131	.9074	.9407	.9562	<b>.9719</b>	.8065	.8669	<b>.8913</b>	.0130	.8719	.8685	.9141	.9352	.6939	.7933	.8157
CTDNet	ACMM 2021	.0138	<b>.9197</b>	.9401	<b>.9620</b>	.9669	.8561	.8682	.8853	.0088	.9190	.9228	.9601	.9646	.8157	.8403	.8610
PFSNet	AAAI 2021	.0149	.9187	.9398	.9528	.9604	<b>.8716</b>	<b>.8964</b>	.8832	<b>.0079</b>	.9233	.9342	<b>.9610</b>	<b>.9659</b>	<b>.8396</b>	<b>.8583</b>	<b>.8705</b>
BSANet	AAAI 2022	<b>.0119</b>	.9170	<b>.9555</b>	<b>.9583</b>	.9635	.8493	.8690	.8873	<b>.0080</b>	.9182	<b>.9513</b>	.9594	.9648	.8147	.8444	.8610
PGNet	CVPR 2022	.0225	.8894	.9105	.9218	.9420	.7921	.8192	.8338	.0153	.8757	.8858	.9178	.9315	.7402	.7775	.7887
DL-based ORSI-SOD methods																	
FSMINet	GRSL2022	.0490	.8343	.8975	.8930	.9007	.7351	.7613	.7804	.0136	.8774	.9038	.9185	.9281	.7165	.7658	.7881
ERPNet	TCYB 2022	.0379	.8655	.9411	.9321	.9530	.8137	.8523	.8791	.0097	.9131	.9211	.9399	.9589	.7453	.8301	.8598
CorrNet	TGRS 2022	.0174	.8949	.9440	.9242	.9421	.8495	.8468	.8516	.0105	.9017	.9448	.9335	.9458	<b>.8193</b>	.8327	.8422
ACCoNet	TGRS 2022	.0173	.8974	.9452	.9575	<b>.9768</b>	.7983	.8359	<b>.9043</b>	.0084	<b>.9268</b>	.9454	<b>.9641</b>	<b>.9705</b>	.8008	<b>.8517</b>	<b>.8810</b>
EMFINet	TGRS 2022	<b>.0116</b>	<b>.9275</b>	<b>.9601</b>	.9556	.9624	<b>.8618</b>	<b>.8780</b>	.8895	<b>.0076</b>	<b>.9241</b>	<b>.9481</b>	.9490	.9596	.8086	.8480	.8663
JRBM	TGRS 2022	.0138	.9182	.9410	.9478	.9633	.7982	.8557	.8854	.0112	.8971	.8947	.9075	.9461	.6967	.7864	.8289
Ours	-	<b>.0095</b>	<b>.9407</b>	<b>.9787</b>	<b>.9747</b>	<b>.9787</b>	<b>.8900</b>	<b>.8981</b>	<b>.9114</b>	<b>.0079</b>	<b>.9293</b>	<b>.9649</b>	<b>.9648</b>	<b>.9690</b>	<b>.8503</b>	<b>.8662</b>	<b>.8805</b>

It can be seen from Table I that the proposed method has certain advantages over other methods on both datasets. Specifically, on the ORSSD dataset, compared with other methods,  $\mathcal{M}$  is reduced by 0.23% to 3.97%,  $S_\alpha$  is increased by 1.36% -25.62%,  $E_\xi^{adp}$  is increased by 1.7% -28.14%, and  $F_\beta^{max}$  is increased by 0.64% -35.16%. Although our method is weaker than ACCoNet in  $E_\xi^{max}$  and  $F_\beta^{max}$  and higher than

EMFINet in  $\mathcal{M}$ , our method significantly outperforms both methods in the other five metrics. For example, compared with ACCoNet and EMFINet,  $S_\alpha$  is increased by 0.25% and 0.52%,  $E_\xi^{adp}$  is increased by 1.95% and 1.68%,  $E_\xi^{mean}$  is increased by 0.07% and 1.58%,  $F_\beta^{adp}$  is increased by 4.96% and 4.18%, and  $F_\beta^{mean}$  is increased by 1.46% and 1.83%. Moreover, we observed that the performance of ORSI-SOD methods is

generally better than that of NSI-SOD methods, which further demonstrates the challenge of the ORSI-SOD task. In particular, as can be seen in the "Publication" column of the table, the methods we have selected for comparison are mostly cutting-edge methods, especially those in ORSI-SOD, and therefore such a comparison is equally challenging. In addition, we also plot the F-measure curve and P-R curve for all methods to

evaluate the performance of the saliency model. In the F-measure curve, the larger the area enclosed by the curve and the coordinate axis, the better the performance of the model. In the P-R curve, the closer the curve is to the (1, 1) coordinate, the better the performance. As can be seen from Fig. 6, our method maintains advantages in both curves compared with other methods.

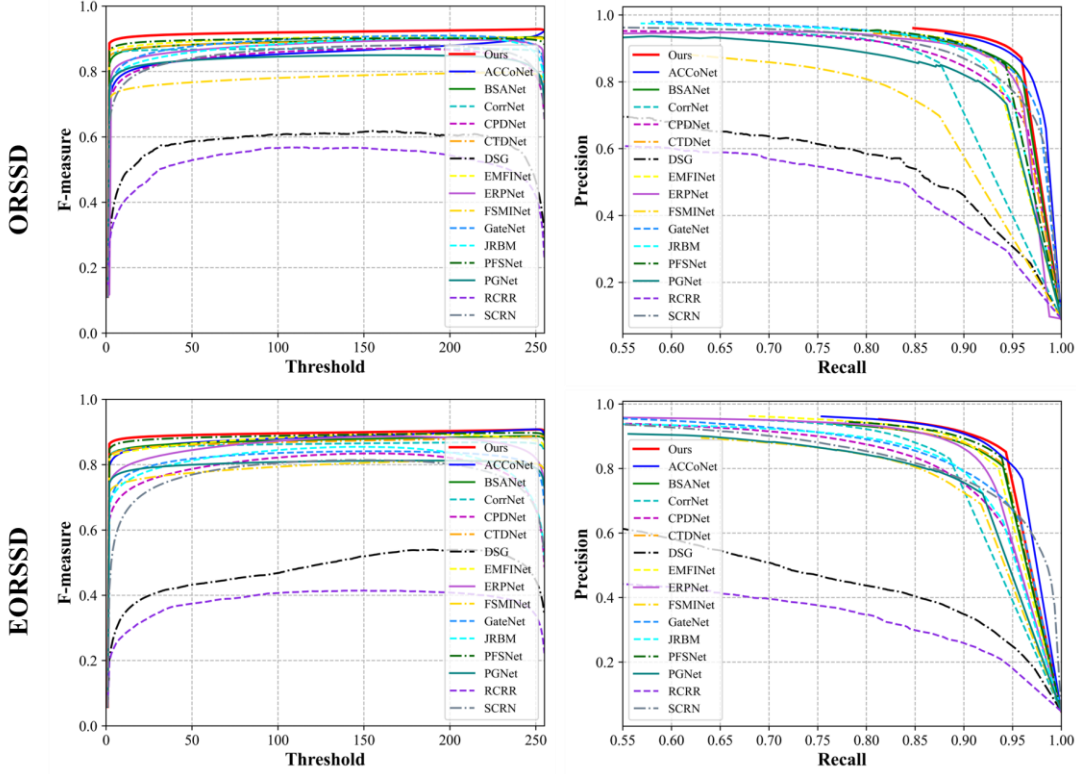


**Fig. 6.** Quantitative comparisons of different saliency models. The first and second rows are PR and F-measure curves, respectively.

(2) *Qualitative Analysis:* In Fig. 7, we show five representative and challenging ORSI scenarios. They are specifically summarized as follows: 1) Three cases of buildings: general building, building with inconsistent colors, and multiple buildings; 2) Three cases of cars: multiple cars, cars with shadows, and cars with complex background; 3) Three cases of planes: general airplane, multiple airplanes, and tiny airplane; 4) Two cases of rivers: river with low contrast and river with irregular topology; 5) Two cases of pools: pool with interferences and pool with complex background. The original images, ground truth, and saliency maps of 16 methods are displayed. It is clear that our method is a more accurate and complete approximation to the ground truth than other methods.

Specifically, in the building detection task, our method clearly distinguishes general buildings and sharply defines the boundary information of buildings; For building with inconsistent colors, our method, CTDNet, PFSNet, and BSA.Net all precisely identify the two buildings. However, the proposed method outperforms the other three in terms of boundary details; For multiple buildings, many methods can accurately distinguish multiple buildings, but their predicted building boundaries will be blurred, while our method can not only clearly distinguish multiple buildings, but also determine the boundary detail information more clearly.

In car detection, for multiple cars, our method and other partial methods can clearly identify multiple cars, but our method is more effective in determining the details of car edge information; For car with shadows, most methods successfully suppress shadow regions, but the proposed method more accurately obtain their structural information and boundary details; Besides, for cars with complex backgrounds, the complex backgrounds are often identified as salient target objects, which create interference for us to detect the target objects. From the sixth row of the figure, it can be seen that PFSNet, ACCoNet, and JRBM can also detect vehicles without being affected by complex backgrounds, but our method outperforms in locating salient objects and description of details.

In airplane detection, for general airplanes, our method can detect the target object completely, while detecting details more accurately than other methods; For multiple airplanes, most methods can detect multiple airplanes, but for airplane boundary information blurred, such as the tail section of the last airplane in the second column of the image in row 8 in Fig. 7, our method reflects this detail well. Besides, for tiny airplanes, it is more difficult to detect for them because the airplanes are relatively small, and our method overcomes this difficulty and has better detection for some details.

In river detection, for low-contrast river, many methods



identify the background as foreground and have incomplete identification of the target, while our method is able to handle this interference well for complete identification of the river; For topologically irregular river, many methods only detect the outer boundary of the river, while only a few methods detect the internal topology of the river, such as PFSNet, BSANet, ACCoNet, but the proposed method is closer to the ground truth for the detection of the boundary and internal topology.

In pool detection, for pool with interference, the proposed

method can still accurately detect the salient object and depict the boundary information clearly even under the condition of intense light changes; For the pool with complex background, our method is not affected by much noise and is able to obtain complete and better bounded saliency targets. In conclusion, our method is able to accurately localize salient objects and delineate fine details in challenging scenes, where it shows strong adaptability and robustness.

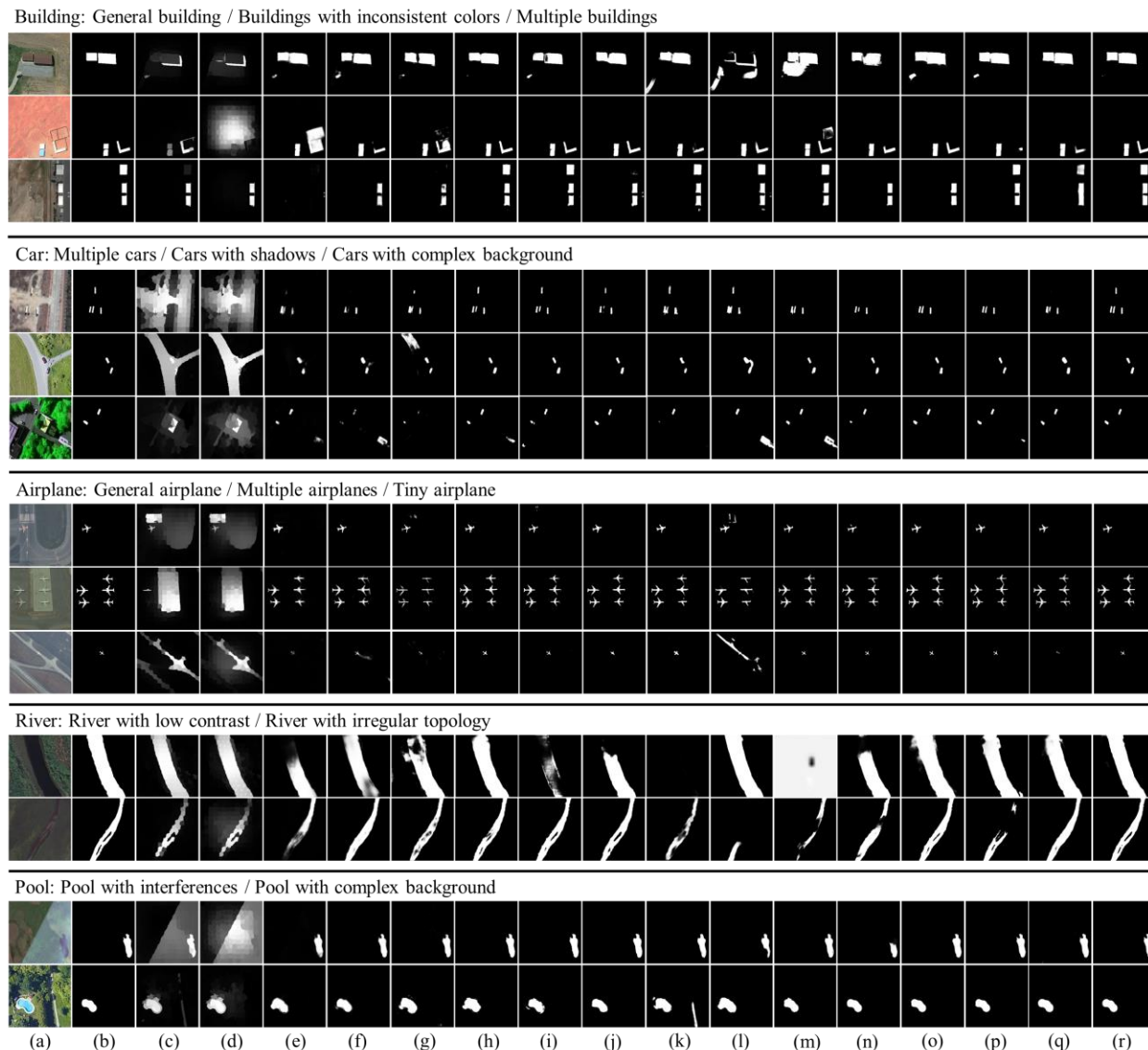


**Fig. 7.** Qualitative analysis of different saliency methods. (a) Optical RSIs. (b) GT. (c) DSG. (d) RCNN. (e) SCRNet. (f) CPDNet. (g) GateNet. (h) CTDNet. (i) PFSNet. (j) BSANet. (k) PGNet. (l) FSMINet. (m) ERPNet. (n) CorrNet. (o) ACCoNet. (p) EMIFNet. (q) JRBM. (r) Ours.

### C. Computational Efficiency Analysis

Considering the comprehensiveness of the proposed method, we further validate the computational efficiency of DFA-BASO. Fig. 8 records three metrics, i.e., FLOPs, Params, and ModelSize, of NSI-SOD and ORSI-SOD methods. It can be clearly seen from the figure that the proposed method still maintains advantages over other methods in these three metrics. Particularly, compared with the current state-of-the-art method ERPNet, our method achieves significantly higher accuracy

while exhibiting lower complexity, fewer parameters, and a smaller model size. It is worth noting that although our method is slightly underpowered compared with the lightest FSMINet, our method also performs far better on both datasets. In addition, we can see from the figure that the three metrics of CPDNet, ACCoNet, and EMIFNet are much higher than our method, but the final accuracy is still not as good as ours. Therefore, in order to obtain such a high accuracy in Table xx, we think it is well worth to sacrifice the complexity, parameters number, and

model size appropriately, and our method achieves an optimal balance between these three metrics and accuracy.

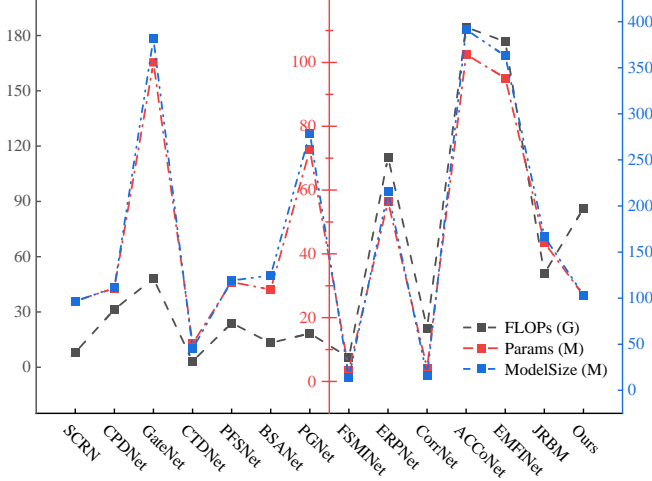


Fig. 8. Computational efficiency analysis of different saliency methods.

In addition to the aforementioned validation, to better apply this method, we analyzed the feasibility of the model by testing its FPS on different devices, as shown in Table II. It can be seen that our method’s FPS on two different devices is acceptable. Similarly, compared with ERPNet, DFA-BASO still has certain advantages in efficiency on different device environments.

TABLE II  
COMPARISON RESULTS OF FPS

Methods	Device Configuration	
	NVIDIA GeForce RTX 3060 8G	NVIDIA GeForce RTX 3090 24G
SCRNet	27.01	49.68
CPDNet	61.08	102.26
GateNet	47.59	110.22
CTDNet	134.69	211.67
PFSNet	40.50	67.76
BSANet	24.43	38.26
PGNet	24.70	43.21
FSMINet	28.01	54.06
ERPNet	21.38	57.61
CorrNet	35.60	74.31
ACCoNet	16.30	38.58
EMFINet	16.89	39.33
JRBM	34.71	54.54
Ours	25.52	59.59

#### D. Ablation Analysis

To effectively demonstrate the contribution of DFA-BASO, this section conducts detailed ablation experiments. Specifically, there are five groups of experiments, including the composition of different components and different loss functions. Table III records the metrics on the ORSSD and EORSSD datasets under different conditions. It is worth noting that for each experiment in this section, we use the same parameter settings as in IV-A(2) and retrain them.

The table reveals that when BPC module is removed (No. 2), there is a 0.1% increase in  $\mathcal{M}$  on ORSSD compared with No. 6, whereas  $E_{\xi}^{max}$  and  $F_{\beta}^{max}$  both decrease by 0.8% and 1.31%, respectively. On EORSSD,  $\mathcal{M}$  increased by 0.03%,  $E_{\xi}^{max}$  decreased by 0.18%. While the performance of  $F_{\beta}^{max}$  is somewhat inadequate, the number of parameters introduced by BPC module is only 0.2M, which is acceptable. And in IV-E, we will further explore its specific contribution to ORSI-SOD. For DFFC module, it can be observed from No. 3 that DFFC introduces only 0.07M parameters and 0.02G FLOPs, and when DFFC module is removed, it results in a 0.55% increase in  $\mathcal{M}$  on ORSSD, and a decrease of 2.71% and 3.23% in  $E_{\xi}^{max}$  and  $F_{\beta}^{max}$ , respectively. On EORSSD,  $\mathcal{M}$  increased by 0.5%, and  $E_{\xi}^{max}$  and  $F_{\beta}^{max}$  decreased by 0.83% and 1.77%, respectively. It can be seen that the performance improvement brought by this module is significant. Additionally, the SSFR module aims at improving the integrity of the final saliency map and has a good contribution to the final performance, as demonstrated by the results in No. 4. When SSFR module is removed, on ORSSD,  $\mathcal{M}$  increased by 0.04%, and  $E_{\xi}^{max}$  and  $F_{\beta}^{max}$  decreased by 0.52% and 0.45%, respectively. On EORSSD,  $\mathcal{M}$  increased by 0.07%, and  $E_{\xi}^{max}$  and  $F_{\beta}^{max}$  decreased by 0.11% and 0.3%, respectively. Finally, for different combinations of loss functions, we only used the standalone BCELoss in No. 5. Due to the lack of IoULoss for global evaluation, the metrics also showed a certain degree of decline. Overall, on the basis of the baseline, the addition of each module brings different degrees of improvement to the final performance. As evidenced by the metrics, the proposed DFA-BASO is meaningful and effective in enhancing performance.

It is worth noting that Table III shows that some modules have only slightly improved certain indicators. To prevent this from being the result of randomness during training, the specific contribution of each module to ORSI-SOD is further analyzed by visualizing feature maps in the next section.

TABLE III  
ABLATION EXPERIMENTAL RESULTS OF DIFFERENT COMPONENTS AND LOSS FUNCTIONS. “B” AND “I” REPRESENT BCELOSS AND IOULOSS RESPECTIVELY. “↑” (↓) MEANS THAT THE LARGER (SMALLER) THE BETTER. THE BEST RESULT IS Bold

No.	Baseline	BPC	DFFC	SSFR	Loss	ORSSD			EORSSD			Complexity	
						$\mathcal{M}$ ↓	$E_{\xi}^{max}$ ↑	$F_{\beta}^{max}$ ↑	$\mathcal{M}$ ↓	$E_{\xi}^{max}$ ↑	$F_{\beta}^{max}$ ↑	Params(M) ↓	FLOPs(G) ↓
1	✓				B+I	.0201	.9442	.8557	.0115	.9456	.8392	25.69	59.53
2	✓		✓	✓	B+I	.0105	.9706	.8983	.0082	.9673	<b>.8814</b>	26.79	72.41

3	✓	✓		✓	B+I	.0150	.9516	.8791	.0094	.9608	.8629	26.92	86.33
4	✓	✓	✓		B+I	.0099	.9735	.9069	.0086	.9680	.8776	26.05	75.09
5	✓	✓	✓	✓	B	.0109	.9738	.9038	.0105	.9652	.8699	26.99	86.35
6	✓	✓	✓	✓	B+I	<b>.0095</b>	<b>.9787</b>	<b>.9114</b>	<b>.0079</b>	<b>.9690</b>	.8805	26.99	86.35

### E. Exploring real contributions of modules

To further confirm the contribution of DFA-BASO to ORSI-SOD, detailed analysis is established by visualizing feature maps. Specifically, in Section III, we conducted a preliminary analysis of the functions of each module, but we believe that the quantitative analysis in IV-D is not enough to fully confirm the real functions of these modules, so we visualized the feature maps after each module to verify whether the contributions of the modules are consistent with those analyzed in Section III.

(1) *Individual contribution of BPC module:* From the preliminary analysis of the BPC module in Section III-B, it can be inferred that this module protects the edge position information in low-level features and alleviates the problem of edge information loss during forward propagation through a level-by-level optimization method. As depicted in Fig. 9, (a1) - (a3) represent the second to fourth layers of the encoder, i.e.,  $E_i \{i = 2, i = 3, i = 4\}$  in Section III-B, while (b1) - (b3) denote the feature maps processed by the BPC module. It is evident from (a1) - (a3) that during the forward propagation of the encoder, the boundary position information becomes increasingly blurred and generates a significant amount of noise, particularly in (a3), the edge information has almost been entirely lost. And after going through the BPC module, the boundary information is protected to some extent in the process of layer-to-layer transmission due to the effective utilization of adjacent features. In addition, the FC sub-module also reduced the noise around salient objects. These optimizations are clearly reflected in (b1) - (b3). Specifically, in (b1) and (b2), the edge information is more accurate and the ambient noise is reduced compared with before calibration (i.e., (a1) and (a2)). In (b3), the contribution of the BPC module is more prominent, and the boundary information is clearly protected. Overall, these visualized feature maps strongly demonstrate the true contribution of the BPC module, which is consistent with the analysis in Section III-B.

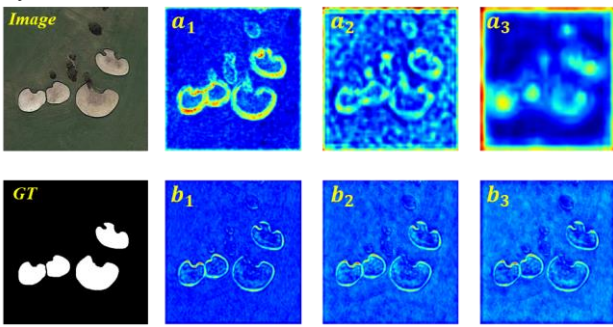


Fig. 9. Illustration of the real contribution of BPC.

(2) *Individual contribution of DFFC module:* The DFFC module, which supplements the features of each layer of the encoder (i.e.,  $E_1 - E_5$ ) through boundary-semantic dual features, is analyzed in section III-C. As shown in Fig. 10, the

obtained dual-feature map (i.e., the Feedback Map in the figure) not only contains rich semantic information but also prevents the boundary information of salient objects from being entirely lost. The attention map with dual features is fed back to each layer of the encoder to supplement the required features and obtain more richer feature maps, as shown in  $G_1 - G_5$ . Specifically, for the lower-level features  $G_1 - G_3$ , the DFFC module not only preserves the edge position information but also suppresses noise while improving the brightness of the internal region of salient objects. In other words, the DFFC module enhances the semantic information inside the salient objects. In  $G_4$ , the DFFC module also suppresses some non-target noise but weakens the semantic information of the salient objects. This is believed to be caused by the ambiguous semantic and localization information about salient objects in  $E_4$ , which make the SELayer uncertain about the target's attention and only preserving weak position information. As the last layer of the encoder,  $E_5$  possesses the strongest semantic information. When receiving feedback, the boundary position information in the feedback map makes the shape of the salient objects closer to the GT, as shown in  $G_5$ . Therefore, the true contribution of the DFFC module is effectively demonstrated through visual feature map presentation.

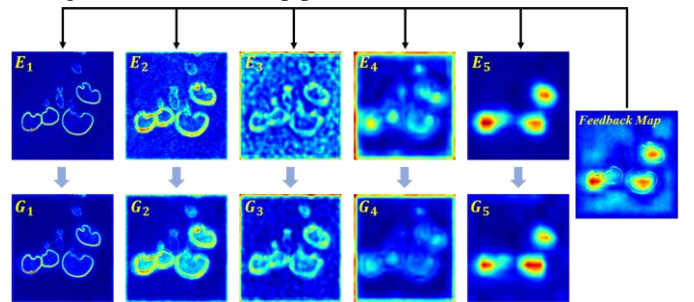


Fig. 10. Illustration of the real contribution of DFFC.

(3) *Individual contribution of SSFR module:* In Section III-D, the SSFR module is introduced to obtain more accurate saliency maps. Fig. 11 shows that as the direct output of the last layer of the decoder,  $D_4$  is highly similar to the ground truth. So, we fed it back to each layer of the decoder and used the submodules described in III-D (2) for feature refinement. "Cross 1" in the figure is the result of crossing " $D_4 + D_1$ " and " $D_4 + D_2$ " after cross refinement. It can be seen that the salient object is more accurately located at this stage, but the accurate judgment of the boundary is still lacking. "Cross 2" is the result of further crossing " $D_4 + D_3$ " and "Cross 1". While the detection of the boundary is clearer, the confidence level for internal area is still low. These problems are solved by information fusion before output, and as seen in the figure, the result of "Fusion" is more accurate than  $D_4$ . The final saliency map is shown as "Output" in the figure. Above all, the analysis of the visualized feature maps strongly proves the necessity of the SSFR module.

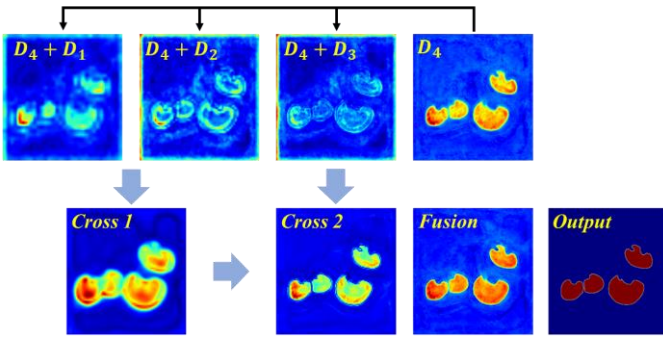


Fig. 11. Illustration of the real contribution of SSFR.

## V. CONCLUSION

In this paper, we investigate the importance of boundary cues for salient object detection and explore the significance of the last layer of the decoder. Subsequently, a novel dedicated method for ORSI-SOD called DFA-BASO is proposed. Considering the loss of boundary information in high-level features, the BPC module is introduced to protect and calibrate the boundary cues, while suppressing the noise in low-level features. In the encoder and decoder, we also adopt two unique feedback mechanisms and propose the DFFC module and SSFR module. The former aims to coordinate the features of each layer in the encoder and achieve feature supplementation, while the latter is used in the decoder to eliminate the feature differences between layers and obtain more refined saliency maps. Finally, extensive experiments, including qualitative and quantitative analysis, computational efficiency analysis, ablation studies, and exploration of real contributions, strongly demonstrate that the DFA-BASO outperforms 15 state-of-the-art methods and significantly improves the performance of ORSI-SOD. Moreover, to facilitate further research, we provide an open-source code repository for SOD.

## REFERENCES

- [1] Wang P, Liu Y, Cao Y, et al. Salient object detection with image-level binary supervision[J]. *Pattern Recognition*, 2022, 129: 108782.
- [2] R. Cong, J. Lei, H. Fu, F. Porikli, Q. Huang, and C. Hou, "Video saliency detection via sparsity-based reconstruction and propagation," *IEEE Trans. Image Process.*, vol. 28, no. 10, pp. 4819–4831, Oct. 2019.
- [3] C. Li et al., "ASIF-Net: Attention steered interweave fusion network for RGB-D salient object detection," *IEEE Trans. Cybern.*, vol. 51, no. 1, pp. 88–100, Jan. 2021.
- [4] P. Zhang, W. Liu, D. Wang, Y. Lei, H. Wang, and H. Lu, "Nonrigid object tracking via deep multi-scale spatial-temporal discriminative saliency maps," *Pattern Recognit.*, vol. 100, Apr. 2020, Art. no. 107130.
- [5] S. Hong et al., "Online tracking by learning discriminative saliency map with convolutional neural network," in *Proc. ICML*, 2015, pp. 597–606.
- [6] K. Gu et al., "Saliency-guided quality assessment of screen content images," *IEEE Trans. Multimedia*, vol. 18, no. 6, pp. 1098–1110, Jun. 2016.
- [7] S. Yang, Q. Jiang, W. Lin, and Y. Wang, "SGDNet: An end-to-end saliency-guided deep neural network for no-reference image quality assessment," in *Proc. 27th ACM Int. Conf. Multimedia*, Oct. 2019, pp. 1383–1391.
- [8] G. Li et al., "Personal fixations-based object segmentation with object localization and boundary preservation," *IEEE Trans. Image Process.*, vol. 30, pp. 1461–1475, 2021.
- [9] G. Li, Z. Liu, R. Shi, and W. Wei, "Constrained fixation point based segmentation via deep neural network," *Neurocomputing*, vol. 368, pp. 180–187, Nov. 2019.
- [10] Bo W, Liu J, Fan X, et al. BASNet: Burned Area Segmentation Network for Real-Time Detection of Damage Maps in Remote Sensing Images[J]. *IEEE Transactions on Geoscience and Remote Sensing*, 2022, 60: 1-13.

- [11] Hua X, Wang X, Rui T, et al. Real-time object detection in remote sensing images based on visual perception and memory reasoning[J]. *Electronics*, 2019, 8(10): 1151.
- [12] D. Zhao, J. Wang, J. Shi, and Z. Jiang, "Sparsity-guided saliency detection for remote sensing images," *J. Appl. Remote Sens.*, vol. 9, no. 1, pp. 1–14, Sep. 2015.
- [13] Zhou L, Yang Z, Zhou Z, et al. Salient region detection using diffusion process on a two-layer sparse graph[J]. *IEEE Transactions on Image Processing*, 2017, 26(12): 5882-5894.
- [14] L. Zhang, Y. Liu, and J. Zhang, "Saliency detection based on selfadaptive multiple feature fusion for remote sensing images," *Int. J. Remote Sens.*, vol. 40, no. 22, pp. 8270–8297, May 2019.
- [15] L. Zhang, S. Wang, and X. Li, "Salient region detection in remote sensing images based on color information content," in *Proc. IEEE IGARSS*, Jul. 2015, pp. 1877–1880.
- [16] Ding L, Wang X, Li D. Visual Saliency Detection in High-Resolution Remote Sensing Images Using Object-Oriented Random Walk Model[J]. *IEEE Journal of Selected Topics in Applied Earth Observations and Remote Sensing*, 2022, 15: 4698-4707.
- [17] Y. Yuan, C. Li, J. Kim, W. Cai and D. D. Feng, "Reversion Correction and Regularized Random Walk Ranking for Saliency Detection," in *IEEE Transactions on Image Processing*, vol. 27, no. 3, pp. 1311-1322, March 2018, doi: 10.1109/TIP.2017.2762422.
- [18] N. Tong, H. Lu, X. Ruan, and M.-H. Yang, "Salient object detection via bootstrap learning," in *Proc. IEEE Conf. Comput. Vis. Pattern Recognit.*, 2015, pp. 1884–1892.
- [19] X. Zhou, Z. Liu, G. Sun, L. Ye, and X. Wang, "Improving saliency detection via multiple kernel boosting and adaptive fusion," *IEEE Signal Process. Lett.*, vol. 23, no. 4, pp. 517–521, Apr. 2016.
- [20] J. Yang and M.-H. Yang, "Top-down visual saliency via joint CRF and dictionary learning," *IEEE Trans. Pattern Anal. Mach. Intell.*, vol. 39, no. 3, pp. 576–588, Mar. 2017.
- [21] K. Fu, I. Y.-H. Gu, and J. Yang, "Saliency detection by fully learning a continuous conditional random field," *IEEE Trans. Multimedia*, vol. 19, no. 7, pp. 1531–1544, Jul. 2017.
- [22] Liu J J, Hou Q, Liu Z A, et al. Poolnet+: Exploring the potential of pooling for salient object detection[J]. *IEEE Transactions on Pattern Analysis and Machine Intelligence*, 2022.
- [23] Wu Y H, Liu Y, Zhang L, et al. EDN: Salient object detection via extremely-downsampled network[J]. *IEEE Transactions on Image Processing*, 2022, 31: 3125-3136.
- [24] Ji Y, Zhang H, Gao F, et al. LGCNet: A local-to-global context-aware feature augmentation network for salient object detection[J]. *Information Sciences*, 2022, 584: 399-416.
- [25] Xu X, Chen J, Zhang H, et al. SA-DPNet: Structure-aware dual pyramid network for salient object detection[J]. *Pattern Recognition*, 2022, 127: 108624.
- [26] C. Li, R. Cong, J. Hou, S. Zhang, Y. Qian, and S. Kwong, "Nested network with two-stream pyramid for salient object detection in optical remote sensing images," *IEEE Trans. Geosci. Remote Sens.*, vol. 57, no. 11, pp. 9156–9166, Nov. 2019.
- [27] Zhou X, Shen K, Weng L, et al. Edge-guided recurrent positioning network for salient object detection in optical remote sensing images[J]. *IEEE Transactions on Cybernetics*, 2022.
- [28] R. Cong et al., "RRNet: Relational reasoning network with parallel multi-scale attention for salient object detection in optical remote sensing images," *IEEE Trans. Geosci. Remote Sens.*, early access, Nov. 1, 2021, doi: 10.1109/TGRS.2021.3123984.
- [29] C. Li et al., "A parallel down-up fusion network for salient object detection in optical remote sensing images," *Neurocomputing*, vol. 415, pp. 120–411, Nov. 2020.
- [30] X. Zhou, K. Shen, Z. Liu, C. Gong, J. Zhang, and C. Yan, "Edgeaware multiscale feature integration network for salient object detection in optical remote sensing images," *IEEE Trans. Geosci. Remote Sens.*, early access, Jul. 5, 2021, doi: 10.1109/TGRS.2021.3091312.
- [31] Q. Zhang et al., "Dense attention fluid network for salient object detection in optical remote sensing images," *IEEE Trans. Image Process.*, vol. 30, pp. 1305–1317, 2021.
- [32] Z. Deng et al., "R3Net: Recurrent residual refinement network for saliency detection," in *Proc. 27th Int. Joint Conf. Artif. Intell.*, Jul. 2018, pp. 684–690.
- [33] X. Qin, Z. Zhang, C. Huang, C. Gao, M. Dehghan, and M. Jagersand, "BASNet: Boundary-aware salient object detection," in *Proc. IEEE/CVF Conf. Comput. Vis. Pattern Recognit. (CVPR)*, Jun. 2019, pp. 7479–7489.
- [34] J. Zhao, J.-J. Liu, D.-P. Fan, Y. Cao, J. Yang, and M.-M. Cheng, "EGNet:

- Edge guidance network for salient object detection,” in Proc. IEEE/CVF Int. Conf. Comput. Vis. (ICCV), Oct. 2019, pp. 8779–8788.
- [35] X. Zhou, K. Shen, Z. Liu, C. Gong, J. Zhang, and C. Yan, “Edge-aware multiscale feature integration network for salient object detection in optical remote sensing images,” *IEEE Trans. Geosci. Remote Sens.*, vol. 60, pp. 1–15, Jan. 2022.
- [36] J.-J. Liu, Q. Hou, M.-M. Cheng, J. Feng, and J. Jiang, “A simple pooling-based design for real-time salient object detection,” in Proc. IEEE/CVF Conf. Comput. Vis. Pattern Recognit. (CVPR), Jun. 2019, pp. 3917–3926.
- [37] G. Li, Z. Liu, W. Lin and H. Ling, “Multi-Content Complementation Network for Salient Object Detection in Optical Remote Sensing Images,” in *IEEE Transactions on Geoscience and Remote Sensing*, vol. 60, pp. 1-13, 2022, Art no. 5614513.
- [38] Hussain R, Karbhari Y, Ijaz MF, Woźniak M, Singh PK, Sarkar R. Revise-Net: Exploiting Reverse Attention Mechanism for Salient Object Detection. *Remote Sensing*. 2021; 13(23):4941.
- [39] Liu Y, Zhang S, Wang Z, et al. Global Perception Network for Salient Object Detection in Remote Sensing Images[J]. *IEEE Transactions on Geoscience and Remote Sensing*, 2022, 60: 1-12.
- [40] Wang Q, Liu Y, Xiong Z, et al. Hybrid Feature Aligned Network for Salient Object Detection in Optical Remote Sensing Imagery[J]. *IEEE Transactions on Geoscience and Remote Sensing*, 2022.
- [41] K. Simonyan and A. Zisserman, “Very deep convolutional networks for large-scale image recognition,” in Proc. 3rd Int. Conf. Learn. Represent. (ICLR), 2015, pp. 1–14.
- [42] L. Itti, C. Koch, and E. Niebur, “A model of saliency-based visual attention for rapid scene analysis,” *IEEE Trans. Pattern Anal. Mach. Intell.*, vol. 20, no. 11, pp. 1254–1259, Nov. 1998.
- [43] J. Ren, X. Gong, L. Y u, W. Zhou, and M. Y . Y ang, “Exploiting global priors for RGB-D saliency detection,” in Proc. IEEE Conf. Comput. Vis. Pattern Recognit. Workshops, 2015, pp. 25–32.
- [44] Q. Wang, Y . Y uan, P. Y an, and X. Li, “Saliency detection by multiple-instance learning,” *IEEE Trans. Cybern.*, vol. 43, no. 2, pp. 660–672, Apr. 2013.
- [45] Y . Wei, F. Wen, W. Zhu, and J. Sun, “Geodesic saliency using background priors,” in Proc. Eur. Conf. Comput. Vis., 2012, pp. 29–42.
- [46] T. Liu et al., “Learning to detect a salient object,” *IEEE Trans. Pattern Anal. Mach. Intell.*, vol. 33, no. 2, pp. 353–367, Feb. 2011.
- [47] H. Jiang, J. Wang, Z. Yuan, Y. Wu, N. Zheng, and S. Li, “Salient object detection: A discriminative regional feature integration approach,” in Proc. IEEE Conf. Comput. Vis. Pattern Recognit., 2013, pp. 2083–2090.
- [48] G. Li and Y . Yu, “Visual saliency based on multiscale deep features,” in Proc. IEEE Conf. Comput. Vis. Pattern Recognit. (CVPR), Jun. 2015, pp. 5455–5463.
- [49] Z. Deng et al., “R3Net: Recurrent residual refinement network for saliency detection,” in Proc. 27th Int. Joint Conf. Artif. Intell., Jul. 2018, pp. 684–690.
- [50] X. Hu, L. Zhu, J. Qin, C.-W. Fu, and P .-A. Heng, “Recurrently aggregating deep features for salient object detection,” in Proc. 32<sup>nd</sup> AAAI Conf. Artif. Intell. (AAAI), 2018, pp. 1–8.
- [51] Z. Wu, L. Su, and Q. Huang, “Cascaded partial decoder for fast and accurate salient object detection,” in Proc. IEEE/CVF Conf. Comput. Vis. Pattern Recognit. (CVPR), Jun. 2019, pp. 3907–3916.
- [52] H. Chen, Y. Li, and D. Su, “Discriminative cross-modal transfer learning and densely cross-level feedback fusion for RGB-D salient object detection,” *IEEE Trans. Cybern.*, vol. 50, no. 11, pp. 4808–4820, Nov. 2020.
- [53] Sun Y, Wang S, Chen C, et al. Boundary-guided camouflaged object detection[J]. *arXiv preprint arXiv:2207.00794*, 2022.
- [54] D. Faur, I. Gavat, and M. Datcu, “Salient remote sensing image segmentation based on rate-distortion measure,” *IEEE Geosci. Remote Sens. Lett.*, vol. 6, no. 4, pp. 855–859, Oct. 2009.
- [55] L. Ma, B. Du, H. Chen, and N. Q. Soomro, “Region-of-interest detection via superpixel-to-pixel saliency analysis for remote sensing image,” *IEEE Geosci. Remote Sens. Lett.*, vol. 13, no. 12, pp. 1752–1756, Dec. 2016.
- [56] Z. Liu, D. Zhao, Z. Shi, and Z. Jiang, “Unsupervised saliency model with color Markov chain for oil tank detection,” *Remote Sens.*, vol. 11, no. 9, p. 1089, 2019.
- [57] C. Dong, J. Liu, F. Xu, and C. Liu, “Ship detection from optical remote sensing images using multi-scale analysis and Fourier HOG descriptor,” *Remote Sens.*, vol. 11, no. 13, p. 1529, Jun. 2019.
- [58] Li G, Liu Z, Zeng D, et al. Adjacent context coordination network for salient object detection in optical remote sensing images[J]. *IEEE Transactions on Cybernetics*, 2022.
- [59] Li G, Liu Z, Bai Z, et al. Lightweight salient object detection in optical remote sensing images via feature correlation[J]. *IEEE Transactions on Geoscience and Remote Sensing*, 2022, 60: 1-12.
- [60] Tu Z, Wang C, Li C, et al. ORSI salient object detection via multiscale joint region and boundary model[J]. *IEEE Transactions on Geoscience and Remote Sensing*, 2021, 60: 1-13.
- [61] Liu Y, Zhang S, Wang Z, et al. Global Perception Network for Salient Object Detection in Remote Sensing Images[J]. *IEEE Transactions on Geoscience and Remote Sensing*, 2022, 60: 1-12.
- [62] Cheng F, Chen C, Wang Y, et al. Learning directional feature maps for cardiac mri segmentation[C]//International Conference on Medical Image Computing and Computer-Assisted Intervention. Springer, Cham, 2020: 108-117.
- [63] Hu J, Shen L, Sun G. Squeeze-and-excitation networks[C]//Proceedings of the IEEE conference on computer vision and pattern recognition. 2018: 7132-7141.
- [64] Lee, C.Y., Xie, S., Gallagher, P., Zhang, Z., Tu, Z., 2014. Deeply-supervised nets. *arXiv 1409.5185*.
- [65] Z. Wu, L. Su, and Q. Huang, “Stacked cross refinement network for edge-aware salient object detection,” in Proc. IEEE Int. Conf. Comput. Vis. (ICCV), Oct. 2019, pp. 7263–7272.
- [66] X. Zhao, Y . Pang, L. Zhang, H. Lu, and L. Zhang, “Suppress and balance: A simple gated network for salient object detection,” in Proc. ECCV, Aug. 2020, pp. 35–51.
- [67] Zhao Z, Xia C, Xie C, et al. Complementary trilateral decoder for fast and accurate salient object detection[C]//Proceedings of the 29th acm international conference on multimedia. 2021: 4967-4975.
- [68] M. Ma, C. Xia, and J. Li, “Pyramidal feature shrinking for salient object detection,” in Proc. AAAI Conf. Artif. Intell. (AAAI), vol. 35, 2021, pp. 2311–2318.
- [69] Zhu H, Li P, Xie H, et al. I can find you! Boundary-guided Separated Attention Network for Camouflaged Object Detection[C]. AAAI, 2022.
- [70] Xie C, Xia C, Ma M, et al. Pyramid Grafting Network for One-Stage High Resolution Saliency Detection[C]//Proceedings of the IEEE/CVF Conference on Computer Vision and Pattern Recognition. 2022: 11717-11726.
- [71] K. Shen, X. Zhou, B. Wan, R. Shi and J. Zhang, "Fully Squeezed Multiscale Inference Network for Fast and Accurate Saliency Detection in Optical Remote-Sensing Images," in *IEEE Geoscience and Remote Sensing Letters*, vol. 19, pp. 1-5, 2022, Art no. 6507705.
- [72] F. Perazzi, P. Krahenbuhl, Y. Pritch, and A. Hornung, “Saliency filters: Contrast based filtering for salient region detection,” in Proc. IEEE Conf. Comput. Vis. Pattern Recognit. (CVPR), Jun. 2012, pp. 733–740.
- [73] D.-P . Fan, M.-M. Cheng, Y . Liu, T. Li, and A. Borji, “Structure-measure: A new way to evaluate foreground maps,” in Proc. IEEE Int. Conf. Comput. Vis. (ICCV), Oct. 2017, pp. 4548–4557.
- [74] D.-P . Fan, C. Gong, Y . Cao, B. Ren, M.-M. Cheng, and A. Borji, “Enhanced-alignment measure for binary foreground map evaluation,” in Proc. 27th Int. Conf. Artif. Intell., Jul. 2018, pp. 698–704.
- [75] R. Achanta, S. Hemami, F. Estrada, and S. Susstrunk, “Frequency-tuned salient region detection,” in Proc. IEEE Conf. Comput. Vis. Pattern Recognit., Jun. 2009, pp. 1597–1604.